

Chapter 1

Foundation of Adaptive Optics

1.1 Introduction

“Twinkle, twinkle, little star,
How I wonder what you are...”

Jane Taylor [1]

The twinkling stars in the night sky stimulated the curiosity of humankind since the beginning of civilization. It was one of the first things which germinated the scientific aptitude in humans. The twinkling and associated blurring very often limits the capability of modern day large optical telescopes of capturing the details of the celestial objects [2]. It is now well understood that the Earth’s atmospheric turbulence along the optical path from any celestial object to a telescope degrades the quality of images by not allowing the telescope to achieve its diffraction-limited angular resolution [3].

As the distances to the astronomical objects are very large, light from any point source reaches above the Earth’s atmosphere as a plane wavefront. In the absence of any atmosphere around the Earth, these plane wavefronts would have reached the telescope unperturbed and formed a perfect diffraction-limited image, in the absence optical aberrations in the telescope itself. However, due to inhomogeneity in the Earth’s atmosphere, refractive index changes rapidly in both space and time. This consequently introduces different travelling speeds at different parts of the plane wavefront leading to distortions of the plane wavefront.

However, the wavefront over the telescope pupil remains correlated over small regions of space for short periods of time with different tilts. This, in turn, produces speckles i.e the image of an object move in space and time at the focal planes of an optical telescope resulting in a blurred image [3] in a long exposure.

To overcome this limitation, two widely adopted approaches are, space telescopes and adaptive optics (AO). In the first approach, the telescope is placed above the earth's atmosphere in orbit around Earth. Thus avoiding the atmosphere altogether to eliminate the turbulence artefacts. However, a space telescope is very costly and hard to maintain. In fact, there are a few working space telescopes at this time operating in optical wavelength, whereas there would be at least 60 ground-based telescopes around the world [3, 4] equipped with adaptive optics. In the adaptive optics approach, however, the distortion in the wavefront due to turbulence is corrected in real-time.

In 1953, Babcock [5] and Vladimir Linik [6] independently proposed the founding concept of the adaptive optics system for the first time. It took almost two decades to realize the first "Real-time wavefront correction system" due to inadequate computing capability [7] and [8].

The fragmented/distorted wavefront produces several images (size of the smallest images, called speckles, is λ/D , where λ , D are wavelength of light and the diameter of the telescope respectively) of the object instantaneously at the focal plane of the telescope. Over a long exposure time, all these tiny images merge together to produce a blurred image. Around any point on the image, the distribution of light or the blurriness follows a Gaussian nature as the speckles form randomly around a point. As a consequence, the size of the sky object in the focal plane become $\approx \lambda/r_0$, where r_0 is the Fried's Parameter [3, 9]. This results in degradation in the resolution by broadening the Point Spread Function (PSF) of the telescope. In short, the atmospheric turbulence severely limits the performance of telescopes, especially when $D > r_0$.

The Full Width at Half Maximum (FWHM) of a blurred image of a point source in the sky, achieved through a turbulent atmosphere is thus, $\approx \lambda/r_0$, [3] which very often is referred to as atmospheric seeing. Due to this reason, all the large telescopes around the world is limited by the atmospheric seeing and their large diameter only helps to collect more photons (and hence to decrease the limiting magnitude) without increasing the resolving power.

1.2 Atmospheric Turbulence

We give a brief account of the atmospheric turbulence and its consequences in optical imaging, in this section. In early twentieth century A. N. Kolmogorov developed the theoretical formalism to model the spatial distribution of three dimensional turbulence [3, 10–13]. In the middle of the twentieth century, Kolmogorov [10] and Obukhov[14] independently worked out the atmospheric turbulence structure function in the inertial subrange which is found to be proportional to $\kappa^{-5/3}$ where κ is the wave number. This is popularly known as the five-third law of turbulence and found to agree very well with observations. An elaborate description of the turbulence theory can be found in the original works of A. N. Kolmogorov¹ [10].

The sun is the dominant source of the heating of the atmosphere. However, solar energy dumped into the atmosphere instigates kinetic energy over a large length-scales. This produces large-scale disturbances or eddies. These are called “outer scale”, L_0 . However, these large-scale eddies are short-lived and quickly break down to small eddies through energy cascading. The large eddies are fragmented to a scale till the viscous forces become significant and dissipate the kinetic energy into heat. This smallest scale is called “inner scale”, l_0 of turbulence. At this stage, the Reynold number (R_e) reduces below to the critical value, and the medium settles in streamline motion. The Reynold number (dimensionless) depends on the velocity (V), characteristic linear dimension/length scale (L) and viscosity (ν) as, $R_e = \frac{VL}{\nu}$. This process produces turbulent eddies of all length-scales $l_0 \leq l \leq L_0$ in a fully-developed turbulent medium. The range is called “inertial range/ inertial subrange”. For atmospheric turbulence, the inner scale, l_0 is found to be of the order of some millimeters whereas the largest scale could be as large as tens of meters.

Through a simple dimensional analysis, Kolmogorov derived the famous two-third law [15] and can be given as,

$$D_v(\xi) = C_v^2 \xi^{\frac{2}{3}} \quad (1.1)$$

¹Original 1941 paper was published in English in 1995

where $D_v(\xi)$ and C_v^2 is the velocity structure function ($\langle |v(r) - v(r + \xi)|^2 \rangle$) and velocity structure constant respectively. The mean square velocity increment between two points separated by a length ξ behaves almost as two-thirds of the power of the length (Equation no 1.1), in turbulent flow at very high Reynolds number. However, this two-third law transforms into a five-third law (Equation no 1.2) in Fourier domain while calculating the spectral energy distribution in a turbulent medium (pg 17 [16]).

$$E_v(\kappa) \propto \xi^{\frac{2}{3}} \kappa^{-\frac{5}{3}} \quad (1.2)$$

Atmospheric Parameters Here, we define and describe in brief the important quantities relevant for adaptive optics (see, e.g., [3].)

1. Coherence length (r_0)

The atmospheric coherence length or Fried's Length (r_0) is defined as the spatial extent of "turbulence cell" over which the RMS optical phase distortion has value ≤ 1 rad. (r_0) can be given as (Equation no 3.51 [3]),

$$r_0 = [0.423 k^2 \sec(z) \int C_N^2(h) dh]^{-3/5}, \quad r_0 \propto \lambda^{6/5} \quad (1.3)$$

where k is wave number of light ($=2\pi/\lambda$) and C_N^2 is the called the index structure coefficient. z and h are the zenith angle and the altitude of the atmospheric layer over which the integration is done respectively.

2. Coherence time (τ_0)

Similar to the coherence length, coherence time (τ_0) is defined as the maximum time duration over which the RMS optical phase distortion remains ≤ 1 rad. It can be given as [3],

$$\tau_0 = 0.314 r_0 / v_{\text{wind}}, \quad \tau_0 \propto \lambda^{6/5}, \quad v_{\text{wind}} = \left[\frac{\int C_N^2(h) v^{\frac{5}{3}} dh}{\int C_N^2(h) dh} \right]^{3/5} \sec(z) \quad (1.4)$$

3. Isoplanatic angle (θ_0)

Similar to coherence length and time, isoplanctic angle (θ_0) also used to indicate the confinement of the phase error. It is the maximum directional angle from the target object which introduces an RMS optical phase distortion of ≤ 1 rad. θ_0 can be given as (Equation no 3.109 [3]),

$$\theta_0 = 0.314 r_0/H, \quad \theta_0 \propto \lambda^{6/5},$$

$$\text{where, } H = \left[\frac{\int C_N^2(h) h^{5/3} dh}{\int C_N^2(h) dh} \right]^{3/5} \sec(z), \text{ mean turbulence altitude} \quad (1.5)$$

1.3 Correction Methods for Ground-Based Telescopes

Here we describe a couple of standard methods used to correct the atmospheric turbulence. Some of the widely used methods are Lucky Imaging [17–19], Tip-Tilt correction [20], Adaptive Optics [5, 6] etc.

1.3.1 Lucky Imaging

Lucky imaging is a post-processing technique for achieving high-resolution image correction for atmospheric seeing. Generally, the average coherence time-scale of the atmospheric turbulence is ~ 10 milliseconds. As turbulence is a statistical phenomena, it is expected that, some of the short-exposure (less than the coherence time) frames would be ‘good enough’ to have a sharp point spread function (PSF). These frames can be considered to have obtained by ‘good luck’. These frames then can be stacked by aligning the centroid of the guiding star (‘shift and add method’, [17, 19]) to produce a effectively long-exposure image. Though this method is capable of producing sharp images with good PSF, the probability of finding a good frame sharply falls as a function of (D/r_o) . Not only that, a significant advancement of CCD technology is the limiting factor for this method, though several recent works have demonstrated it very effectively [18, 21–25]. N.M. Law et al. (2006) [26] succeeded to have the first Airy ring at a radius of $0.1''$ under $0.42''$ seeing in I band at 2.56 m Nordic Optical Telescope in this passive technique.

1.3.2 Tip-Tilt Correction System

Noll [27] observed that the low order aberration of the wavefront, i.e. atmospheric tilt account for $\sim 87\%$ of the phase variance for a telescope of aperture radius equal to the Fried parameter. In that sense, the quality of an image can be improved greatly just by correcting the low order aberration, i.e., tip-tilt in real time using a tip-tilt staged mirror. The tip-tilt mirror could be placed at the pupil plane or at the adaptive optics secondary [20] which introduces an equivalent tip-tilt (in the opposite direction) into the incoming light beam. Using this correction, it is possible to reduce the phase errors substantially in the infrared regime as the turbulence effect is less at longer wavelengths. Phase errors due to tip-tilt, set the image into motion in the detector plane, which can be traced by a high-speed detector. A correction factor then can be computed and introduced to the tip-tilt mirror's stage to nullify the motion of the image due to the said phase error. It should be noted that all these are performed in real time, i.e., within the coherence time.

In IUCAA Girawaly Observatory (IGO) the Near Infrared Picnic Imager (NIPI) instrument was designed for the tip-tilt correction in real time (see [28] for more details). Roddier [29] has shown that the image size reduces by one-half at $1.2 \mu\text{m}$ in a 4-m class telescope just for low-order tip-tilt correction. Jim [30] demonstrated $0.3''$ FWHM image resolution in K band at University of Hawaii 2.2 m telescope using tip-tilt correction.

1.3.3 Adaptive Optics

An adaptive optics system probes and corrects the wavefront phase error, higher order aberrations for the finer fluctuations as well as low order tip-tilt in real time.

An adaptive optics system can enhance the performances of the ground-based telescopes significantly. In recent years, several 1-3 m class telescopes have been upgraded with adaptive optics system. For example, Mount Wilson, Lick Observatory, P60 of Palomar Observatory, 2m telescope of Kitt Peak National Observatory and many others have implemented an adaptive optics backend to improve the PSF. Though the development of AO systems took nearly four decades, in coming times, almost all the optical observatories would be equipped with the AO

system. In the following subsections, we present a more detailed description of the primary components and their working principle of an adaptive optics system.

1.3.3.1 Introduction

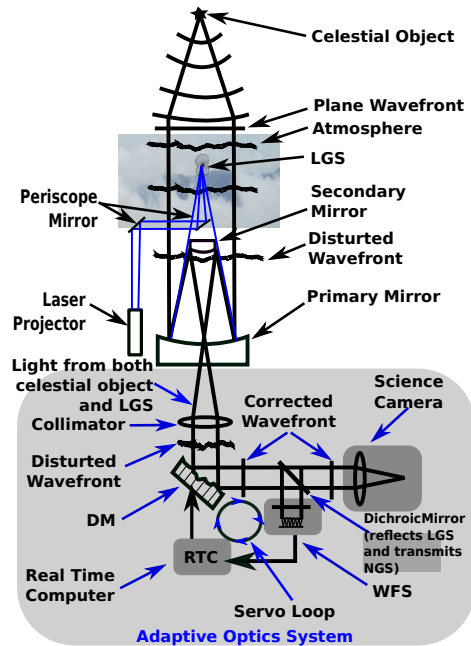


FIGURE 1.1: Schematic layout of telescope and Adaptive Optics system.

An AO system employs a multi-variable servo loop to correct the distortions in the incoming wave-front in real time [31, 32]. It measures the distorted wave-front coming from the sky by a sub-system called wave-front sensor and sends signals to computer controlled actuators of the deformable mirror for wavefront correction. These actuator driven deformable mirror then introduces physical path differences which compensate for the phase errors introduced by the atmospheric turbulence. The lower order tip-tilt aberration introduces the maximum phase error, which requires a higher degree of the dynamic range of the actuators of the deformable mirror. Such degree of dynamic range with high accuracy, repeatability very often is hard to achieve with present-day technology. This large aberration is often corrected by a flat mirror attached to a tip-tilt platform. However, wavefront measurement demands a bright guide star very close to the target star (within isoplanatic angle) for the adequate signal to noise ratio. The probability of getting a star fulfilling the criteria of a guide star (a bright enough source within the

isoplanatic field around the target star) is very low especially above the galactic plane ([33]).

To overcome this, one can employ an artificial guide star created by shooting a high-intensity laser aligned to the optical axis of the telescope as suggested by Foy et al. 1985 ([33]). A schematic diagram of the whole AO setup is shown in Figure 1.1.

1.3.3.2 Wave-Front Sensors (WFS)

Measurement of the distortions introduced to the incoming plane wave-front is one of the most important requirements needed to perform a correction in real time. Hence, wave-front sensors have got deserving attention in the last decades or so. As a result, several wave-front sensing schemes have emerged, e.g., shearing interferometry, pyramid wavefront sensor, Curvature sensors, Shack-Hartmann (SH) etc. Amongst these, the pyramid wavefront sensor and SHWFS are most popular, and we discuss them below in some more detail.

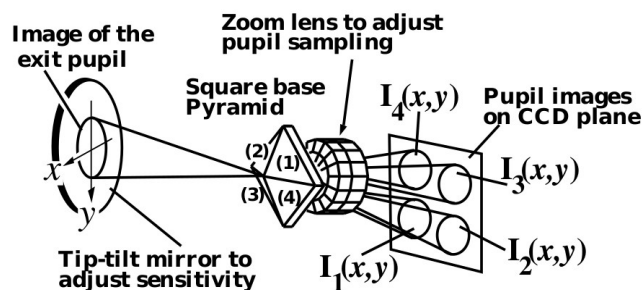


FIGURE 1.2: Schematic layout of Pyramid Wavefront Sensor[34]

Pyramid Wavefront Sensor: Ragazzoni developed the first pyramid wavefront sensor almost two decades ago [35]. In Figure 1.2 we present a schematic of a pyramid wavefront sensor. As it can be seen from the figure, it is constructed out of a glass pyramid having a square base [34]. The vertex of the pyramid is placed at the focal plane of the telescope. Using a relay lens system, four images of the exit pupil are constructed on the CCD detector. Consequently, the pyramid split the light beam from the sky into four parts. Each part produces individual images of the telescope pupil at the CCD detector. There are multiple pixels in CCD constructing the individual images of the pupils coming from the splitted

beam. Each of these pixels is a sub-aperture. Hence, in this pyramid system, each sub-aperture has four counterparts. In other words, each sub-aperture is detected in four pixels in the CCD. The slope of the wavefront in x and y direction are expressed as a function [36] of counts of the said four pixels in Equation 1.6,

$$\begin{aligned} \frac{\partial W(x, y)}{\partial x} &\propto \frac{[I_1(x, y) + I_4(x, y)] - [I_2(x, y) + I_3(x, y)]}{[I_1(x, y) + I_2(x, y) + I_3(x, y) + I_4(x, y)]} \\ \frac{\partial W(x, y)}{\partial y} &\propto \frac{[I_1(x, y) + I_2(x, y)] - [I_3(x, y) + I_4(x, y)]}{[I_1(x, y) + I_2(x, y) + I_3(x, y) + I_4(x, y)]} \end{aligned} \quad (1.6)$$

where $W(x, y)$ and $I_{1,2,3,4}(x, y)$ are the wavefront and the pixel counts of the four pixels of an identical subaperture marked in Figure 1.2.

There a number of instruments which implemented a pyramid wavefront sensor for AO corrections, for example, Multi-Conjugate Adaptive Optics Demonstrator (MAD) [37] and LINC Nirvana [38] etc.

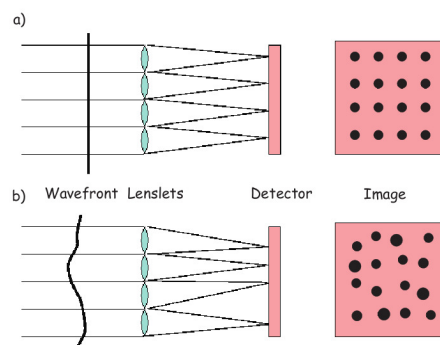


FIGURE 1.3: Image formed in the focal plane by Shack-Hartmann lenslet array: (a) regular grid for undistorted image and (b) shifting of convergence points proportional to the slopes of the wavefront.

[39, 40]

Shack-Hartmann wavefront sensor (SHWFS): Shack-Hartmann wavefront sensor (SHWFS) is one of the simplest wavefront sensor which provides a reasonably good characterization of the incoming wave. Earlier a Hartmann mask (opaque mask containing arrays of holes) was used for ray tracing for the calculation of merit figure of large telescopes as well as a tool for focusing telescopes. Later Ronald Shack replaced the holes of the Hartmann masks with tiny lenses [41] to measure the wavefront. With a slight modification, the Hartmann aperture

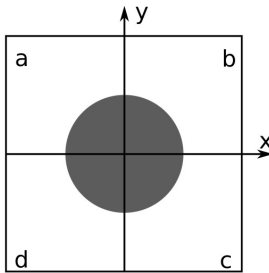


FIGURE 1.4: Pictorial representation of a spot on a quadcell.

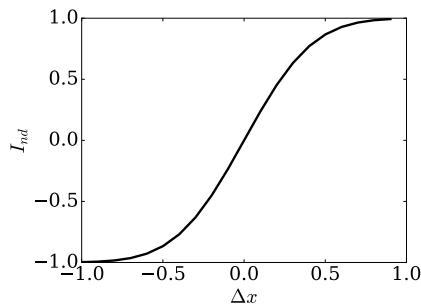


FIGURE 1.5: Quad cell response, ‘S’ based on Equation no 1.8, without approximation (STD: 0.333).

turned into a continuous array of lenslets without any space in between. The continuous array of lenslets minimizes light loss and hence maximises the efficiency of the system (see Figure 1.3). For a collimated beam parallel to the optical axis of the system (parallel to the optical axis of the lenslets), each lenslet forms a ‘spot’ at its focal plane on axis.

However, due to atmospheric turbulence, if there are a gradients in the phase across the wavefront of the light beam, the position of the spots will be shifted. In other words, the shift of the centroids of the ‘spots’ (of the lenslets) is a measure of the distortion of the incoming wavefront. With this matrix of the spot centroids, one can calculate the distribution of the phase errors across the wavefront of the beam and the correction needed to compensate the same. However, it should be noted that, determination of all the centroids and corresponding corrections for the phase errors should be done in real time and hence is computationally challenging. The measurement of the centroid is done using a quad cell and discussed below.

Quad cell: Determination of the centroid is one of the key steps which should be performed with accuracy in minimum time. It should be noted that all these computations must finish quicker than the coherence time. Hence, an efficient algorithm for locating the centroids of the spots is an absolute requirement. The performance of the Shack-Hartmann wavefront sensor is limited by photon noise and the read noise. Read noise is minimised by reducing the number of detectors. Thus the quad cell approach which is one of the simplest ones in which the ‘spot’ is sampled by 2×2 pixels is commonly used for ‘slope’ detection.

The spot is sampled by 2×2 pixels, named as a, b, c and d in Figure 1.4, the intensities in each pixel are denoted by I_a , I_b , I_c and I_d . In quad cell method, the centroid of the spot can be given as [42],

$$c_x = \sigma \sqrt{\pi/2} \frac{(I_b + I_c) - (I_a + I_d)}{I_a + I_b + I_c + I_d}, \quad c_y = \sigma \sqrt{\pi/2} \frac{(I_a + I_b) - (I_c + I_d)}{I_a + I_b + I_c + I_d} \quad (1.7)$$

The quad cell response is like ‘S’ shaped (Figure 1.5) ².

Hence the output needs to be adjusted to get actual centroid shifts. A pre-determined look-up table is often used to estimate the actual shift of the centroids out of the ‘S’ shaped quad cell response. An optimization on the relative size of the quad cell and the spot is carried out to avoid any possible saturation. For example, ideally, the spot size should fit in a single pixel and fall close to the center of the quad cell. If the focal lengths of the SHWFS lenslet is f and M is the magnification between the lenslet plane and the telescope pupil, slope of the wavefront (the average angle) to the optical axis at the pupil plane can be given as

$$S_x = \frac{c_x}{fM}, S_y = \frac{c_y}{fM} \quad (1.10)$$

The wavefront reconstruction from the slope measurement is given in the section 1.3.3.4.

²Let us assume the spot on the quad cell is Gaussian $Ae^{-\frac{x^2+y^2}{2\sigma^2}}$. We can see [42],

$$I_{total} = \sum_{i=a,b,c,d} I_i = A \int_{y=-\infty}^{\infty} \int_{x=-\infty}^{\infty} \exp\left(-\frac{x^2+y^2}{2\sigma^2}\right) dx dy = A\sigma^2 (2\pi) \quad (1.8)$$

$$\Delta I(c_x) = A\sigma^2 2\sqrt{\pi} \int_{x=0}^{\frac{c_x}{\sigma\sqrt{2}}} \exp(-a^2) da$$

$$I_{nd} = \frac{(I_b + I_c) - (I_a + I_d)}{I_a + I_b + I_c + I_d} = \frac{2\Delta I(c_x)}{I_{total}} = \frac{2}{\sqrt{\pi}} \int_{x=0}^{\frac{c_x}{\sigma\sqrt{2}}} \exp(-a^2) da \quad (1.9)$$

Where the $\Delta I(c_x)$ term corresponds to the magnitude of intensity change by shifting the intensity distribution to a new mean c_x . I_{nd} is the normalised intensity difference. The ‘S’ response (Figure 1.5) is plotted using Equation 1.9.

1.3.3.3 Deformable Mirrors

Once, the wavefront sensor determines the phase errors across the incoming wavefront, the next step is to correct these phase errors. This is done by one or more Deformable Mirrors (DM). In Figure 1.6, we show the basic working of a DM by a schematic diagram. As can be seen from the figure, the incoming light beam gets reflected from the DM and hence, travels the same distance twice. The plane wave reflects back from the DM, if the DM surface profile is kept half of the surface profile of the incident wavefront. Depending on the technology, a wide range of different sizes of deformable mirrors are available. The size of the mirrors could vary from a few mm to the order of meters (large secondary mirror) [43, 44] depending on its location and optical relay. Not only that, there are different types of actuators also available with different technologies (e.g., Stacked array DM, Bimorph DM, Voice-coil actuator, micro-electromechanical system (MEMS) etc. [39, 44]). Here we give a brief description of MEMS DM which we have used for our instrument for IGO observatory.

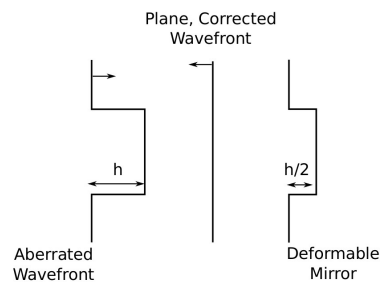


FIGURE 1.6: DM and wavefront surface profile.

MEMS-DM The recent advancement of the Micro-Electro-Mechanical System (MEMS) technology has revolutionised the development of low-cost high-density DM systems [44]. These systems are produced by a batch processing technique used in silicon industry grade integrated circuit development (IC). The actuators could be densely packed with the size of a few micrometres to millimetres. As a result, these devices are capable of controlling the actuating action on micro-scales to generate an effect on macro-scale. As one of the first demonstrations, Boston Micromachines Corporation fabricated MEMS-based DMs surface by micro-machining of the poly-silicon thin film in 2012 [46].

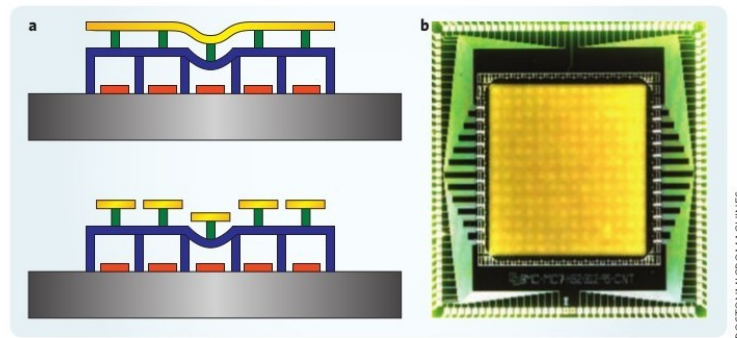


FIGURE 1.7: Design of MEMS DMs. (a) Cross-section of continuous (upper) and segmented (lower) MEMS DMs. The parts are coloured for identification. **Gold:** A metal-coated thin-film mirror. It is attached to silicon posts. **Green:** An array silicon posts. Locally anchored to the electrostatic actuator membranes. **Blue:** Electrostatic actuator membranes. **Red:** An array of rigid silicon static actuator electrodes. **Grey:** The wafer substrate. (b) Photograph of a fabricated DM with 140 active actuators (and two inactive buffer rings) supporting a continuous DM (Taken from Fig 1 of [45])

A very thin layer is placed to isolate the conductive layers between. Selective etching is generally used to build up the actuator structure (see e.g., [47] for more details). The individual actuators are addressed (or controlled) through channels wire-bonded to a ceramic carrier. However, the DM surface is attached to a movable membrane by a post. A thin reflective coating of gold is used to make the reflecting surface of the DM. The movable actuator membrane is placed on top of static electrodes, which decides the dynamic range of the DM. An applied voltage to the electrodes induces an electrostatic force between the membrane and the electrodes, which in turn drive the movement of the membrane. The deflection on the membrane due to this electrostatic force is proportional to the square of the applied voltage.

1.3.3.4 Wavefront Reconstruction

The Wavefront Reconstructor process calculates the entire wavefront over the pupil using the slope input from the WFS and translates into the required displacements for correction to be applied to the DM. The calculations of the displacements are to be done in real-time (quicker than the coherence time) and should be implemented using efficiently optimized algorithms. It is found that an algebraic approach using matrix formulation is suitable for this operation.

If there are m numbers of phase values, W_m to be restored with n numbers of measurements, S_n , then a linear relation can be established in matrix form,

$$W_{m \times 1} = R_{m \times n} S_{n \times 1} \quad (1.11)$$

where R is the reconstruction matrix which should be known to solve the above equation. Two methods are widely used to reconstruct the wavefront [3, 31]. The first one is called ‘modal’, assuming the wavefront can be decomposed into orthonormal polynomials and the second one is ‘zonal’ which employs the geometry of the WFS and DM actuators to compute the phase errors. We only discuss the Modal reconstruction technique [3] here, as we use this technique in IGO AO system.

Modal Wavefront Reconstruction: In this method, a wavefront can be assumed to be made up of N independent orthonormal polynomial basis (Zernike, Disc-Harmonics[48] etc.)

$$W(x, y) = \sum_{k=1}^N a_k Z_k(x, y) \quad (1.12)$$

where a_k is the coefficient of the k^{th} orthonormal polynomial, Z_k . Given this, the slope of the wave front in x and y direction can be given as,

$$S^x(x, y) = \frac{\partial}{\partial x} W(x, y), \quad S^y(x, y) = \frac{\partial}{\partial y} W(x, y) \quad (1.13)$$

However, in practice, the measurement of this slope is not continuous and only measured at the sub-aperture locations. Hence, the above equation should be discretised at i^{th} sub-aperture. In a zonal wavefront sensor like the SHWFS, the slope measurements are made over the subaperture. Let the index of all the subapertures at the location i is (x_i, y_i) . The measured slopes at the i^{th} location can be represented as

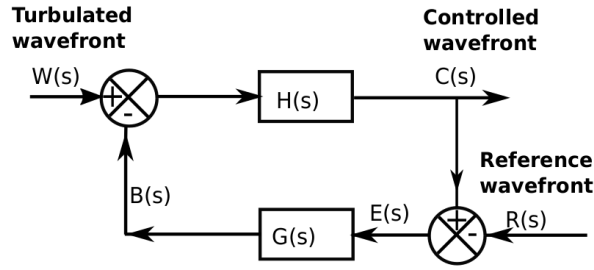


FIGURE 1.8: Basic Control System for an Adaptive Optics system

$$\begin{aligned}
 S_i^x(x, y) &= \frac{\partial}{\partial x} W_i(x, y) = \sum_{i=1}^N a_i \frac{\partial}{\partial x} Z_i(x, y), \\
 S_i^y(x, y) &= \frac{\partial}{\partial y} W_i(x, y) = \sum_{i=1}^N a_i \frac{\partial}{\partial y} Z_i(x, y)
 \end{aligned}
 \tag{1.14}$$

Equation 5.4 can be further formalized in matrix form to compute the coefficients of the orthonormal polynomials as,

$$S = A a \tag{1.15}$$

where A is the interaction matrix consists of the derivatives of the basis polynomial functions. The solutions of ‘ a ’ can be obtained employing Least-square estimator technique as [40, 49, 50],

$$a = (A^t A)^{-1} A^t S = R S \tag{1.16}$$

where ‘ R ’ is the reconstruction matrix. Thus, the coefficient array ‘ a ’ can be calculated from the measured gradients, ‘ S ’ and consequently, the phase values can be estimated using Equation 1.12.

1.3.3.5 Control System

The control system is a very important connection between the wavefront sensor and the wavefront corrector in an adaptive optics system. There are various

techniques in which this control function can be achieved. The most well-known method is a negative feedback loop. In this method, the incoming wavefront is at first compensated by the wavefront corrector (DM). Then the residual error is calculated after the compensation; then a control signal is fed back to the wavefront corrector, which is proportional (in the simple case, proportional control system) to the error signal with the appropriate polarity to null the error.

A typical adaptive optics control system is shown in Figure 1.8 [3, 32]. The basic motto of the control system is to make the controlled wavefront $[C(s)]$, same as the reference wavefront $[R(s)]$ in the presence of the turbulent wavefront $W(s)$.

In the context of the AO system, the wavefront sensor measures the controlled wavefront and compares with reference then produces an error signal $E(s)$. The error signal $E(s)$ is multiplied with a transfer function $G(s)$ to produce a signal $B(s)$ which should be exactly identical with input wavefront $W(s)$, so that the output wavefront $C(s)$ will exactly follow the reference wavefront $[R(s)]$ value. If the $C(s)$ does not follow $R(s)$ then an error signal $E(s)$ is generated to neutralize the $W(s)$ to get $R(s)$ as the controlled wavefront.

1.3.3.6 Laser Guide Star

Estimating the phase errors in the wavefront is very critical to compute the corrections for the AO system. Hence, it must be determined with a sufficiently high degree of accuracy. For this reason, the detection of the ‘spots’ with high SNR is necessary. Hence, a bright guide star near the target source (within the isoplanatic patch) is required to perform the wavefront sensing well. However, the availability of bright sources is not high enough to have a bright guide star inside the isoplanatic patch of a target across all sky. To overcome this limitation, R.Foy and A. Labeyrie [33] proposed an alternative by creating an artificial guide star in the sky using a laser. Earth’s atmosphere contains dust particles at lower altitudes and sodium at higher altitudes. Mie scattering from dust, Rayleigh scattering from molecules or resonance scattering from sodium atoms return sufficient amount of light so as to create a bright source in the upper atmosphere, as a guide star. As the Laser Guide Star (LGS) remains within the isoplanatic angle, it probes the almost identical patch of the sky as the target source. However, as this LGS is formed at a finite height (unlike a natural guide star which is at an infinite distance), there is some amount of error in the wavefront measurement called cone

effect. There is a trade-off between the low SNR of guide star and the cone effect. It is to be mentioned that the cone effect error decreases with a high ratio of the height of the LGS and the telescope's aperture size.

To receive LGS photons from a chosen height in the atmosphere, one can use a Range Gate system in front of the WFS. Range Gate is a shutter that can selectively allow photons over a certain time window coming from a particular height to reach the WFS. Presently, Sodium and Rayleigh-type LGS are used in AO systems. For Sodium LGS ($0.589\mu\text{m}$), the light gets backscattered from the Mesosphere which is at a height of $\sim 80 - 100$ km from the mean sea level. Not only that, the thickness of the layer is $\sim 10 - 20$ km which provides a superb cross-section for back-scattering through a resonance fluorescence process. Because this scattering happens at very high altitude, the cone effect for a Sodium LGS is minimal. For LGS created by Rayleigh scattering, the LGS forms at a height of $\sim 8 - 15$ km. In this case, the cone effect is more serious and hence Rayleigh LGS can be used only in small telescopes.

1.3.4 Brief History of AO Developments

Around 1950, Babcock[5] and Vladimir Linik[6] independently conceived the concept of adaptive optics. It took another three decades to start the hands on experiments of an AO system due to technology limitations of computers, detectors, deformable mirrors etc. The first attempts for the AO correction was made for the military applications. With the advancement of computers, deformable mirrors, fast readout CCDs etc, the last three decades witnessed development and operation of around sixty adaptive optics programmes all over the world. Now the technology has become mature enough to handle much more complex and high-speed AO systems for large telescopes like Giant Magellan Telescope(GMT, 25m), Thirty Meter Telescope(TMT, 30m), Extremely Large Telescope(ELT, 39.3m) etc. through the pathfinding projects on the smaller telescopes. The entire effort for this technology is to achieve high photon sensitivity and angular resolution of a telescope, often close to diffraction limited performance. Several observatories have upgraded their telescopes with AO facility.

Here we have done a brief review of a few AO systems and their performance[3, 4].

1.3.4.1 Small-Medium Sized Telescope AO

There are several medium and small-sized telescopes which have deployed AO systems. These include the Canada-French-Hawaii Telescope (CFHT) which is a 3.6 m optical, infrared telescope located at the summit of Mauna Kea[51], 60 inch(Coude) and 100 inch(Cassegrain) telescope at Mt Wilson[52], 1.04 m telescope at Yerkes Observatory, Shane 3 m telescope at Lick Observatory[53], Palomar observatory 60 inch, Kitt-Peak observatory 2 m telescope etc. The Lick AO system is briefly described below.

Lick Observatory (3 m)

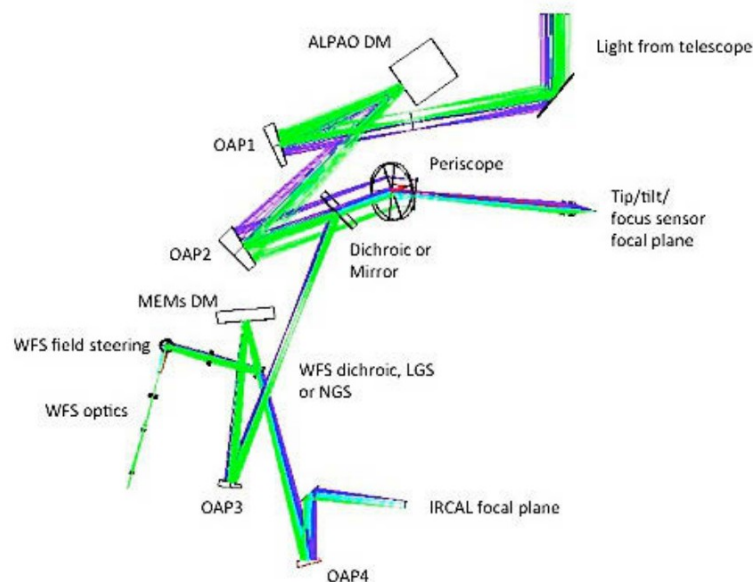


FIGURE 1.9: Lick AO system Optical Layout (Taken from [53])

The largest telescope at the Lick Observatory is a 3 m Shane Reflector telescope, which from 2001 has offered an Adaptive Optics facility to users. The Shane AO system achieve diffraction limited imaging over the infrared band (0.8 to 2.2 μm) with a high Strehl ratio. The AO system is detailed in Gavel et al.[53]. The optical layout of the AO system is given in Figure 1.9. The AO system is mounted at the Cassegrain focus of the telescope, and is briefly described below.

The system has two deformable mirrors. The first deformable mirror (called woofer) corrects low order aberrations, including tip/tilt. It is a magnetically

actuated membrane mirror with 52 elements. It has a stroke up to $\pm 50 \mu\text{m}$. This mirror removes need for a separate tip/tilt mirror. It also eliminates the need for a fast steering stage on which DM is usually mounted for tip-tilt correction. There is a dichroic mirror which splits the woofer light, sending $600 \text{ nm} < \lambda < 900 \text{ nm}$ light over a $120''$ field to the tip/tilt sensor and the central $20''$ field on to a second relay. The second relay is a narrow-field ($20''$) one, with the pupil conjugated at second DM which is MEMS-based. The MEMS DM is a 1020-actuator KILO-DM produced by Boston Micromachines Corporation. It has negligible hysteresis. There are roughly 30 actuators across the beam diameter. There is a field stop in front of the wavefront sensor. It blocks the Rayleigh backscatter photons from low altitudes from fogging the wavefront sensor. The aperture size is around the field of view of the subapertures on the wavefront sensor CCD, $\approx 6''$ diameter. The field stop has an opening at the center of a broad blackened disk. It also suppresses any stray reflection back into the sensor. A collimated beam is incident on the Shack-Hartmann wavefront sensor which is placed after the MEMS deformable mirror and the WFS dichroic. The WFS dichroic splits and sends light at $\lambda < 1\mu\text{m}$. It allows both NGS as well as LGS mode. In LGS mode, the laser guide star return at $\lambda = 589 \text{ nm}$ and in NGS mode starlight at $\lambda < 900 \text{ nm}$. In NGS mode, the dichroic in the first relay is removed, and a mirror is used to measure the atmospheric turbulence at the wavefront sensor. Note that the first TTM sensor is not used, and the signal for tip-tilt is derived from the WFS and goes to the first DM. In LGS mode, the dichroic in the first relay sends the LGS light and the target star's light towards the second DM. The wavefront sensing recollimated beam through a field stop hits the lenslet array. The array of focused dots are relayed using relay optics to the wavefront sensor camera. Two sets of Hartmann collimator/lenslet/relay assemblies are used to switch the wavefront measurement performance between a low and high-resolution mode. The low-resolution mode contains eight lenslets across the pupil diameter, i.e. 40 cm subapertures at the primary. The low-resolution mode is useful for sensing faint natural guide stars and the LGS. The high-resolution mode has 15 lenslets across the pupil diameter i.e. 20 cm subapertures at the primary. It is beneficial for producing higher Strehls at the shorter science wavelengths but would need a brighter guide star. Lincoln Laboratories CCID66 array was employed for the wavefront sensor detector. It is an array of 120×120 pixels with 1-2 e^- read noise at up to 1.5 kHz frame rate. SciMeasure Analytical Systems built the camera controller.

Shane AO system could resolve the $0.4''$ separated stars (such as a portion of the M92 globular cluster) in the H band under normal seeing conditions.

1.3.4.2 Operational AO system on Large Telescopes

Gemini Observatory (Two 8.1 m)

Now AO is an integral part of Gemini telescopes (two identical 8.1 m telescopes).

Gemini North: ALTAIR (ALTitude conjugated Adaptive optics system for the Infrared Red), is offered to Gemini North and available for use with both natural and laser guide stars. ALTAIR accepts f/16 beam and produces the same beam f/16 to feed Near InfraRed Imager (NIRI) and Near InfraRed Integral Field Spectrometer (NIFS). It has one Deformable mirror consists of 177 actuators conjugated to the turbulent layer height of 6.5 km. A separate mirror is used for tip-tilt correction. 12×12 lenslet Shack-Hartmann wave-front sensor (WFS) is employed for the wavefront measurement. The correction loop works at a rate of up to 1 kHz. [54–56]

It achieved[55] 73 mas FWHM images in K band.

Gemini South: The main adaptive optics system in Gemini South is the GeMs, the Gemini Multi-Conjugate Adaptive Optics System[57, 58].

It has five laser guide stars which are distributed at the corners and center $60''$ square. These 5 LGS are produced by splitting in 5×10 of a 50 watt laser and feed five 16×16 subapertures Shack-Hartmann WFSs. There are total 2040 slope measurements are used to compute the MCAO high-order correction. It corrects by two deformable mirrors which are conjugated to 0 and 9 km at up to 800 Hz. Tip-tilt measurements are done using up to three visible natural guide stars for the compensation of the tip-tilt and anisoplanatic modes.

GeMS obtained[58] images with FWHM of $0.08''$ or better over a field of view $85'' \times 85''$ under median seeing, or better with an average Strehl ratio of 17% in H band. In general, it delivers a quite uniform, near diffraction limited images in the near-infrared bands ($0.95 - 2.5 \mu m$) over a field of view of $120''$.

Subaru (8.2 m)

The Subaru telescope (8.2 m optical-infrared telescope) at the summit of Mauna Kea, Hawaii is operated by National Astronomical Observatory of Japan (NAOJ).

The main Laser Guide Star Adaptive Optics system in Subaru is AO188 system[59–61]. It has curvature WFS system (CWFS) with fiber coupled 188 photon counting Avalanche Photodiode (APD) modules. The WFS updates at 2 kHz. The 2×2 visible SHWFS with 16 photon counting APDs or an infrared SHWFS with a HgCdTe array measures the tip-tilt and defocus. A 188 element electrode bimorph mirror is used. The DM is mounted within a fast tip/tilt mount. The system generates laser guide star[62] using 4-10 W solid-state sum-frequency laser.

The adaptive optics system AO188 has delivered image quality close to the diffraction limit; the FWHM is 55 mas in H band under $0.6''$ natural seeing[63].

European Southern Observatory (Four 8.2 m)

The European Southern Observatory (ESO) developed several AO systems like COME-ON[64], COME-ON+[65], ADONIS[66], Multi Application Curvature Adaptive Optics (MACAO-VLTIs)[67], Multi-Conjugate Adaptive Optics Demonstrator (MAD)[37] etc. Here a brief description of MAD is given.

The ESO built a MAD[37] for demonstrating adaptive optics correction over a wide field of view. The MAD instrument is installed on a single bench, which now is fitted at the Nasmyth-B platform of the Very Large Telescope (VLT) UT-3 unit. There are two deformable mirrors for correction of two layers of the atmosphere. The MAD has a 100 mm DM, conjugated to the altitude of 8.5 Km and a 60 mm DM conjugated to the telescope pupil. The telescope pupil conjugated DM is mounted on a Tip-Tilt Mount for ground layer tip-tilt correction. MAD uses both modal and zonal reconstruction approaches for wavefront reconstruction.

MAD registered in GLAO mode Strehl Ratio in K band $\approx 8\%$ under $0.85''$ seeing condition uniformly over a $1'$ field of view[68].

Keck Observatory (Two 10 m)

These are two identical 10 m telescopes separated by a distance of 85 m at the William M. Keck Observatory (WMKO), located on the summit of Mauna Kea in Hawaii[69].

Each Keck telescope is on an altitude-azimuth mount with the AO system on a Nasmyth platform[70]. Multiple sodium resonance laser guide stars perform tomographic wavefront sensing[71]. Keck AO uses a Shack-Hartmann lenslet array made of 20×20 square lenslets as the wavefront sensor. A total of 304 subapertures cover the pupil. The wavefront is reconstructed by 240 subapertures which are full illuminated out of the 304 subapertures. There is field rotation[72] on the science camera as the telescope tracks a star due to the alt-azimuth mount. This is compensated by an image rotator which is placed before the AO system. But there is a rotation of the pupil[72] with time. A new calculation of the reconstruction matrix triggered after every one degree rotation of the pupil. Singular value decomposition algorithm is used to perform the influence matrix inversion[73].

Keck delivered[72] images with a Strehl ratio around 0.37 at $1.58 \mu\text{m}$ when a bright natural guide star (natural guide star mode) was used and the Strehl ratio was 0.19 with 12 magnitude guide star.

1.3.4.3 Future Large Telescope AO

AO systems are an integral part of all the upcoming large telescopes and are integrated from the beginning of their design. Upcoming large telescopes like GMT[74], TMT[75] etc. are ground-based optical telescopes based on segmented mirror technology. Adaptive optics systems are incorporated as an integral part of these telescopes to achieve their full performance.

GMT[76] uses six beacons (Sodium Resonance, 120 watt of 589 nm laser) from the periphery of the primary mirror for LGS facility. It has segmented adaptive secondary mirror for AO correction. Natural Guide Star AO (NGSAO) and Laser Tomography AO(LTAO) modes included to provide diffraction-limited image quality over $0.9\text{-}25 \mu\text{m}$ wavelength range.

TMT AO[77] is a Multi-conjugate AO with two DMs, six Laser guide stars (Sodium Resonance). The natural guide stars take care of the tip-tilt correction in NIR band. TMT AO is designed to have diffraction-limited image quality in near IR over a field-of-view of $10\text{-}30$ arcsec.

1.4 Outline of the thesis

Overall, in this thesis, a detailed description of the design, development and commissioning of the iRobo-AO system is presented. In the Chapter 2, the design and development of the Cassegrain box is discussed. In Chapter 3, we discuss the Laser Guide Star system whereas, in Chapter 4, the atmospheric dispersion corrector is presented. Chapter 5 presents an extension of the currently developed iRobo-AO system, i.e., the Near Infra-Red (NIR) camera. The commissioning of the system is detailed in Chapter 6. Finally, in Chapter 7, summary and potential future work are presented.